Han Xiao (Orcid ID: 0000-0001-8727-8053)
Toshiro Tanimoto (Orcid ID: 0000-0001-6980-5075)
Zack J. Spica (Orcid ID: 0000-0002-9259-1973)
Beatriz Gaite (Orcid ID: 0000-0002-7542-8795)
Sandra Ruiz-Barajas (Orcid ID: 0000-0001-7981-6392)
Mohan Pan (Orcid ID: 0000-0003-0445-6462)
Loïc Viens (Orcid ID: 0000-0002-7975-7799)

# Locating the precise sources of high-frequency microseisms using distributed acoustic sensing

**Han Xiao[1]*, Toshiro Tanimoto[1], Zack J. Spica[2], Beatriz Gaite[3], Sandra Ruiz-Barajas[3], Mohan Pan[4], Loïc Viens[2]**

[1]Department of Earth Science and Earth Research Institute, University of California, Santa Barbara, Santa Barbara, USA.

[2]Department of Earth and Environmental Sciences, University of Michigan, Ann Arbor, USA.

[3]National Geographic Institute of Spain, Madrid, Spain.

[4]OBS Lab, Department of Ocean Science and Engineering, Southern University of Science and Technology, Shenzhen, China.

*Corresponding author. Email: hanxiao@ucsb.edu

## Key points:

- A fiber-optic cable on the seafloor is used to locate the sources of high-frequency microseisms with an unprecedented precision
- The sources of high-frequency microseisms quickly move within narrow areas of a few kilometers
- The constantly changing source locations are most likely related to the ephemeral behaviors of wind

## Abstract

Although microseisms have been observed for more than 100 years, the precise locations of their excitation sources in the oceans are still elusive. Underwater Distributed Acoustic Sensing (DAS) brings new opportunities to study microseism generation mechanisms. Using DAS data off the coast of Valencia, Spain, and applying a cross-correlation approach, we show that the sources of high-frequency microseisms (0.5-2 Hz) are confined between 7 and 27 km from the shore, where the water depth varies from 25 to 100 m. Over time, we observe that these sources move quickly

This is the author manuscript accepted for publication and has undergone full peer review but has not been through the copyediting, typesetting, pagination and proofreading process, which may lead to differences between this version and the Version of Record. Please cite this article as doi: 10.1029/2022GL099292.

along narrow areas, sometimes within a few kilometers. Our methodology applied to DAS data allows us to characterize microseisms with a high spatiotemporal resolution, providing a new way of understanding these global and complex seismic phenomena happening in the oceans.

## Plain Language Summary

Microseisms are a type of seismic noise that is ubiquitous on Earth and has been studied for over 100 years. However, we still have no way of knowing exactly where it is generated in the ocean. Recent advances in underwater fiber-optic sensing bring a tremendous opportunity to better understand the source mechanism of microseisms. We use seafloor Distributed Acoustic Sensing (DAS) data to achieve for the first time a precise localization of the noise sources of high-frequency microseisms. We found that the sources of high-frequency microseisms are very narrow, often only a few kilometers. Moreover, the noise source area is constantly changing with the wind direction.

## 1. Introduction

There is a long history of studying ambient seismic noise, especially the predominant ocean-generated microseisms (Hasselmann, 1963; Longuet-Higgins, 1950; Wiechert, 1904). It is well established that there are two main frequency bands that are referred to as the primary (0.05-0.07 Hz) and secondary microseisms (0.13-0.40 Hz) (Hasselmann, 1963; Le Pape et al., 2021; Longuet-Higgins, 1950; Retailleau & Gualtieri, 2021; Tanimoto, 2007; Toksöz & Lacoss, 1968; Xiao et al., 2018). The primary microseisms are generated by direct coupling between ocean waves and seafloor topography in shallow ocean regions (Ardhuin et al., 2015; Hasselmann, 1963). And the secondary microseisms could be generated by the interaction of waves in opposite directions from different storms in the deep ocean or by the interaction of reflected and incident waves close to the coast (Ardhuin et al., 2011). Previous terrestrial research observations have shown that typically very little secondary microseism energy from the deep ocean reaches continental stations and terrestrial observations are dominated by nearshore wave activity (Bromirski et al., 2013), especially for the short-period microseisms (Koper & Burlacu, 2015). Other evidence shows the arrivals of teleseismic signals at about 0.2 Hz that are generated by far-away storms mix with locally generated secondary microseisms (Kedar et al., 2008; Nishida & Takagi, 2016). Microseisms can excite both surface and body waves (Koper et al., 2010; Nishida & Takagi, 2016; Retailleau & Gualtieri, 2021; Xiao et al., 2021), which are extensively used to explore and monitor the Earth's interior at all scales through cross-correlations (Brenguier, Campillo, et al., 2008; Brenguier, Shapiro, et al., 2008; Denolle et al., 2014; Poli et al., 2012; Shapiro et al., 2005). Thus far, the lack of high-density offshore seismic observations prevented seismologists from fully characterizing the complexity of microseisms. We can now move beyond this limitation using distributed acoustic sensing (DAS) and existing underwater telecommunication infrastructures (Guerin et al., 2022; Lindsey et al., 2019; Sladen et al., 2019; Spica, Nishida, et al., 2020; Williams et al., 2019).

DAS is a new method to measure the Earth's vibrations with an unprecedented resolution. It uses the optical phase changes of Rayleigh backscattered light to turn fiber-optic cables into dense arrays of seismic sensors measuring dynamic longitudinal strain or strain rate. At the end of the

fiber, an interrogator unit (IU) sends laser pulses down the cable. The propagation of the laser pulses is affected by heterogeneities in the fiber and some of the energy travels back to the IU. When the fiber is disturbed by external forcing, phase changes of the backscattered light are measured by the IU and can be turned into continuous strain measurements along the fiber with a very high spatial resolution (Muanenda, 2018; Posey et al., 2000). For an extensive review of the DAS technology, we refer the reader to Hartog (2017).

In this study, DAS data were recorded along a sea-bottom cable linking Valencia to Palma de Mallorca, Spain (Figure 1a)(Spica, Gaite, et al., 2020). By using a method based on short-term cross-correlation functions, we achieved for the first-time precise localization of the microseism sources. We report our observations on the variations of microseism source locations at frequencies of 0.5-2.0 Hz. To distinguish this high-frequency signal from the well-known microseisms, we use the term "the High-Frequency microseisms (HF microseisms)" in this study. Actually, the source of HF secondary microseism is ubiquitous (Gal et al., 2017; Pyle et al., 2015). Previous research has suggested that the HF secondary microseism source location may be nearshore as it correlates with nearby offshore wind speeds (Zhang et al., 2009).

Data are discussed in section 2, the locating results and modal analyses of HF microseism in section 3, and the close relation between microseism sources with wind directions is discussed and concluded in section 4.

## 2. Data

### (2.1) DAS experiment

We used a pre-installed telecommunication fiber-optic cable operated by IslaLink that connects the Spanish peninsula to Mallorca Island from Valencia to Palma de Mallorca (Figure 1a). From September 1st to September 15th, 2020, a FEBUS Optics A1-R interrogator was connected to the Valencia side of the cable to probe the first 50 kilometers of the cable (Spica, Gaite, et al., 2020). While the total length of the cable is longer than 50 km, the maximum distance that can be probed with DAS is limited by the power of the laser, which rapidly attenuates with distance (Lindsey et al., 2019; Spica, Nishida, et al., 2020; Williams et al., 2019). The initial 8,555 meters of the cable are located on land, and the following 41,445 meters are under the seabed. According to the installation report provided by the cable operator, the cable is buried ~1 m below the seabed for the full length of the measurement. The data were acquired with a sampling frequency of 1000 Hz, a gauge length of 30.4 m, and a spatial resolution of 16.8 m, turning the first 50 km of the cable into a dense seismic array of 2977 channels. We only analyze the data recorded between September 1st and September 7th, which are continuous, and exclusively focus on the underwater portion of the cable.

### (2.2) Wind and ocean waves data

Waves and wind model data are also used in this study to explain our measurements and are obtained from the Spanish Ports Authority database (Puertos del Estado), called SIMAR (SImulación MARina in Spanish). SIMAR comes from WANA and is based on WAM (Group, 1988) and WaveWatch III (Tolman, 2009). Over the years, the WANA has been improving the

temporal and spatial resolution of the model, and the current temporal and spatial resolutions are one hour and 2.1 km, respectively. The model parameters used in this study are waves peak period, waves mean coming-from direction, and wind coming-from direction.

# 3. Results

### (3.1) Ocean surface gravity waves and Scholte waves

Each channel exhibits two energy peaks in the frequency domain (Figure 1b). The first peak has a frequency band of 0.05-0.2 Hz. It is mainly observed in shallow waters, and its power decreases with increasing water depth. The same signal can be observed in the frequency-wave number analysis (Figure S1a) and travels with a phase velocity of ~10 m/s. This corresponds to the propagation of ocean surface gravity waves in the shallow waters, which directly exert pressure on the fiber-optic cable (Lindsey et al., 2019; Sladen et al., 2019; Spica, Nishida, et al., 2020; Williams et al., 2019). The second peak is found in the 0.5-2 Hz frequency band. This signal travels with a phase velocity of 500-1000 m/s (Figure S1b) and corresponds to the propagation of the fundamental-mode Scholte waves (Supplementary material and Figures S2-S4), whose energy is essentially trapped under the seabed (Lindsey et al., 2019; Nishida, 2017; Nolet & Dorman, 1996; Scholte, 1958; Sladen et al., 2019; Spica, Nishida, et al., 2020; Williams et al., 2019).

Figure 1c shows 40 seconds of the strain rate data filtered between 0.5 and 1 Hz. The propagations of the HF microseisms are revealed through oblique stripes traveling either up to the right toward the land (i.e., landward) or propagating seaward down to the right. In addition, Figure 1d shows that ocean waves that propagate in opposite directions mainly occur in the 0.25-0.5 Hz frequency range (period 2-4 s in Figure 1d), which approximately corresponds to approximately the double-frequency relationship between the microseism signals and the ocean waves. The modal analysis (Supplementary material and Figures S2-S6) supports that the wave-wave interactions of ocean surface waves generate the wavefield recorded at the seabed which dominates the HF microseisms (Longuet-Higgins, 1950).

### (3.2) The sources of HF microseisms

To better understand the wavefield created by the HF microseisms, we computed cross-correlation functions (CCFs) of DAS data between each channel (virtual source) and a receiver channel located 1.5 km (i.e., 90 channels) away. To increase the stability of the CCF signals, we first stacked the raw strain-rate data of five adjacent channels. Then, we compute the CCFs with the following five stacked channels located 1.5 km away. In the CCFs, we identify acausal (negative) and causal (positive) wave packets propagating landward and seaward, respectively. These are the same propagating waves observed in Figure 1c. The correlation technique allows us to track the propagation directions of the HF microseisms (Figures 2a and 2b). Due to the strong energy of this signal, we found that stable CCFs are obtained for time series as short as 10 minutes. These 10-minute CCFs match the 6-day-long stacked CCFs (Figures 2a and 2b), implying that Scholte waves are propagating parallel to the fiber. Therefore, we used the 10-minute-long time series to increase the temporal resolution of the phenomena captured by the CCFs. We computed the CCFs between all channel pairs spaced by 1.5 km for each 10-minute time series. Therefore, for every 10 minutes, it provides us with 2374 CCF results for the entire 2468 DAS channels along the seabed.

We used the signal-to-noise ratio (SNR) of CCFs to evaluate the existence and significance of HF microseisms. The SNR was computed by taking the maximum amplitudes of the CCF signals, independently for the acausal part and the causal part, and taking their ratio to the noise amplitude. The noise amplitude was estimated from the average amplitude in the trailing CCF coda for a duration of 200 sec (Figure S7). Figure 2a is an example of CCF that clearly shows the landward propagation of HF microseism (acausal part in red) with an SNR of 12.3. The wave propagation of waves toward the deeper sea (causal part in blue) is, however, unclear even though SNR is 3.1. Figure 2b is a case in which there are clear seaward signals but not a hint of landward propagation. In this case, the SNR is 9.8 for seaward propagation and 3.2 for landward propagation. In general, the SNR is larger than 4.0 when we see a recognizable wave packet in the CCFs. Figure 2c shows the results for all the CCFs computed for all 10-minute intervals over the entire six days and expressed as a function of their SNR for both landward (red) and seaward propagation (blue).

Figure 2c illustrates that between 0 and 7 km from the coast, the causal part of the CCFs (i.e., blue lines) exhibit an overall SNR lower than 3, which means that there is no significant seaward wave propagation. However, the landward propagating signals are much larger. On the other hand, beyond ~27 km from the coastline, seaward wave propagation becomes dominant. The landward propagating signals show SNR under 4, suggesting that the wavefield beyond 27 km is dominated by HF microseisms propagating toward the deeper sea. Until now, the excitation source of HF microseisms was assumed to emit seismic waves propagating in both the landward and seaward directions from the source (Ardhuin & Herbers, 2013; Hasselmann, 1963; Longuet-Higgins, 1950; Tanimoto, 2007). However, the patterns in Figure 2c suggest that the source regions of the HF microseism are mostly confined within 7-27 km from the coast and the sources can radiate seismic waves in either landward or seaward direction and/or both.

**(3.3) Spatiotemporal variations of HF microseisms sources**

To see the temporal fluctuation of the sources, Figures 3a and 3b show the SNR results as a function of time. For every 10-minute interval, the SNR of seaward and landward signals are plotted from left to right for about six days with respect to the distance from the coast. This figure shows that SNR patterns change rapidly in time, meaning that the source locations are constantly moving. Sometimes, the source is all the way out to 25 km from the coast (black circle on Sept. 2). This indicates that the landward propagation dominates the wavefield. On Sept. 3 (green circle), the wavefield mostly consists of seaward propagation, which means that the excitation source is about 10 km from the coast. Most of the time, the source seems to be somewhere between 15 and 20 km from the coast (pink circle). It is important to recognize that the position of the HF microseism sources is constantly changing, and the extent of the source is relatively small for a given time instance. In this study, for the first time, we have realized the positioning of the surface wave HF microseism, and the positioning error is only a few kilometers, so we call it high-precision positioning.

By putting the variations of SNR in Figures 3a and 3b in a single plot, we can constrain the source locations for the frequency band 0.5-1 Hz (Figure 4a). The positions between the two-color regions (red and blue) must be the source location because away from the source, the SNR of the landward (red) propagating wave should become smaller toward the deeper sea, and the SNR of seaward

(blue) should become smaller toward the coast. This range cannot be determined precisely, but in Figure 4b, we show a case where we treat the region of SNR larger than 5 in both landward and seaward propagations as the source region. The orange area shows the source extent, which oscillates in time and space. For each time instance, the spatial extent of the source is limited to an area of a few kilometers to 10 km. A similar analysis was applied to HF microseisms for a higher frequency band 1-2 Hz (Figure S8) and shows that the timing of changes in source location mostly agrees with those in Figure 4b. These results depend on the threshold selection of SNR equal to 5, and a different choice would provide broader or narrower estimates of the source region. Nonetheless, in most cases, the extent of the source region appears to be limited to a strip of 10 kilometers, most often within a few kilometers. The source area is constantly changing within the 7-27 km region from the coast, which is where the bathymetry varies from 25 to 100 m in depth. However, in Figure 1b, the noise amplitude is higher outside the noise source area, such as 5-7 km and beyond 27 km from the coast. We believe that the noise amplitude is related to the velocity of the subsurface structure, as can be seen from Figure S9, the S-wave velocity is higher at 10-20 km, and the velocity is lower at 5-7 km and beyond 30 km from the coast. And previous work on microseisms found that for noise amplitude, the amplification effect of the sedimentary basin is far more important than the proximity to the noise source (Koper & Burlacu, 2015). Therefore, amplification effects by shallow sedimentary layer are likely responsible for the larger noise amplitude.

## 4. Conclusions

How can we explain such changes in the excitation source of HF microseisms? We theorize that wave-wave interaction of ocean waves, generated by local winds, can explain these behaviors. As Figure 1d shows, the dominant period range of opposing winds is 2-4 seconds. Through the frequency doubling process from the collision of opposing ocean waves (Ardhuin et al., 2011; Hasselmann, 1963; Longuet-Higgins, 1950; Tanimoto, 2007), they can create the seismic wavefield in the 0.5-1.0 Hz range found in our data. A modal analysis shows that this process preferentially excites the fundamental-mode surface waves (Figure S5). This mode corresponds to the Scholte waves as the maximum displacements occur at the sea bottom (Figure S4) and decay upward and downward from the seabed. Its large horizontal amplitude indicates an efficient excitation of extensional strain, which is the primary signal in DAS data. The constantly changing source locations are most likely related to the ephemeral behaviors of the wind and its related ocean waves (black line in Figure 4a). Locations of wave-wave interactions should naturally change if the wind were the source of this process.

The water depth must be an influential parameter as shown in modal analysis, and thus the efficiency of excitation of such modes can change significantly concerning depth. A relatively flat and shallow Mediterranean seabed with a depth range of 25-100 m may have played a prevailing role in our observations. Excitation of the HF microseisms should differ under different bathymetric conditions. Nevertheless, more quantitative modeling of the noise source distribution should be performed in the future to better understand our observations.

The results of this study reveal that DAS will soon play a significant role in understanding the excitation mechanisms of microseisms.

## Acknowledgments

We thank IslaLink Holding Iberia S.L. for providing access to the BalaLink underwater fibre infrastructure. We are grateful to the Spanish National Geographic Institute and the Spanish Seismic Network for cooperation and data transfer. We thank Gaëtan Calbris from Febus Optics for his swift help on the field.

## Contributions

H.X. conceived and designed the experiment, analyzed data, and wrote the initial manuscript. T.T. did the modal analysis, contributed to writing, and supervised the project. Z.J.S. collected the DAS data, coordinated the project, and provided critical assistance to the analysis. B.G. and S.R.B. helped to record the DAS data. M.P. visualized the results. L.V. independently verified the results. All authors contributed to the manuscript.

## Data Availability

The DAS data necessary to reproduce all results and figures in this article can be obtained from Spica, Gaite, et al. (2020). (https://doi.org/10.7914/SN/ZH_2020). The wind and waves data were obtained from the website of the Spanish Ports Authority database (https://www.puertos.es/en-us/oceanografia/Pages/portus.aspx).

## References


Ardhuin, F., Gualtieri, L., & Stutzmann, E. (2015). How ocean waves rock the Earth: Two mechanisms explain microseisms with periods 3 to 300 s. *Geophysical Research Letters, 42*(3), 765-772. https://doi.org/10.1002/2014GL062782

Ardhuin, F., & Herbers, T. H. C. (2013). Noise generation in the solid Earth, oceans and atmosphere, from nonlinear interacting surface gravity waves in finite depth. *Journal of Fluid Mechanics, 716*, 316-348. https://doi.org/10.1017/jfm.2012.548

Ardhuin, F., Stutzmann, E., Schimmel, M., & Mangeney, A. (2011). Ocean wave sources of seismic noise. *Journal of Geophysical Research, 116*(C09004). https://doi.org/10.1029/2011JC006952

Brenguier, F., Campillo, M., Hadziioannou, C., Shapiro, N. M., Nadeau, R. M., & Larose, E. (2008). Postseismic Relaxation Along the San Andreas Fault at Parkfield from Continuous Seismological Observations. *Science, 321*(5895), 1478-1481. https://doi.org/10.1126/science.1160943

Brenguier, F., Shapiro, N. M., Campillo, M., Ferrazzini, V., Duputel, Z., Coutant, O., & Nercessian, A. (2008). Towards forecasting volcanic eruptions using seismic noise. *Nature Geoscience, 1*(2), 126-130. https://doi.org/10.1038/ngeo104

Bromirski, P. D., Stephen, R. A., & Gerstoft, P. (2013). Are deep-ocean-generated surface-wave microseisms observed on land? *Journal of Geophysical Research: Solid Earth, 118*(7), 3610-3629. https://agupubs.onlinelibrary.wiley.com/doi/abs/10.1002/jgrb.50268

Capon, J. (1969). High-resolution frequency-wavenumber spectrum analysis. *Proceedings of the IEEE, 57*(8), 1408-1418.

Dahlen, F. A., & Tromp, J. (2021). Princeton University Press. https://doi.org/10.1515/9780691216157

Denolle, M. A., Dunham, E. M., Prieto, G. A., & Beroza, G. C. (2014). Strong Ground Motion Prediction Using Virtual Earthquakes. *Science, 343*(6169), 399-403. https://doi.org/10.1126/science.1245678

Group, T. W. (1988). The WAM Model—A Third Generation Ocean Wave Prediction Model. *Journal of Physical Oceanography, 18*(12), 1775-1810. https://journals.ametsoc.org/view/journals/phoc/18/12/1520-0485_1988_018_1775_twmtgo_2_0_co_2.xml

Guerin, G., Rivet, D., van den Ende, M. P. A., Stutzmann, E., Sladen, A., & Ampuero, J.-P. (2022). Quantifying microseismic noise generation from coastal reflection of gravity waves recorded by seafloor DAS. *Geophysical Journal International*. https://doi.org/10.1093/gji/ggac200

Hartog, A. H. (2017). *An introduction to distributed optical fibre sensors*, CRC press.

Hasselmann, K. (1963). A statistical analysis of the generation of microseisms. *Reviews of Geophysics, 1*(2), 177-210. https://doi.org/10.1029/RG001i002p00177

Kedar, S., Longuet-Higgins, M., Webb, F., Graham, N., Clayton, R., & Jones, C. (2008). The origin of deep ocean microseisms in the North Atlantic Ocean. *Proceedings of the Royal Society A: Mathematical, Physical and Engineering Sciences, 464*(2091), 777-793. https://doi.org/10.1098/rspa.2007.0277

Koper, K. D., & Burlacu, R. (2015). The fine structure of double-frequency microseisms recorded by seismometers in North America. *Journal of Geophysical Research: Solid Earth, 120*(3), 1677-1691. https://doi.org/10.1002/2014JB011820

Koper, K. D., Seats, K., & Benz, H. (2010). On the composition of Earth's short-period seismic noise field. *Bulletin of the Seismological Society of America, 100*(2), 606-617. https://doi.org/10.1785/0120090120

Le Pape, F., Craig, D., & Bean, C. J. (2021). How deep ocean-land coupling controls the generation of secondary microseism Love waves. *Nature Communications, 12*(1), 2332. https://doi.org/10.1038/s41467-021-22591-5

Lindsey, N. J., Dawe, T. C., & Ajo-Franklin, J. B. (2019). Illuminating seafloor faults and ocean dynamics with dark fiber distributed acoustic sensing. *Science, 366*(6469), 1103-1107. https://doi.org/10.1126/science.aay5881

Longuet-Higgins, M. S. (1950). A Theory of the Origin of Microseisms. *Philosophical Transactions of the Royal Society of London A-Mathematical and Physical Sciences, 243*(857), 1-35. https://doi.org/10.1098/rsta.1950.0012

Muanenda, Y. (2018). Recent Advances in Distributed Acoustic Sensing Based on Phase-Sensitive Optical Time Domain Reflectometry. *Journal of Sensors, 2018*, 3897873. https://doi.org/10.1155/2018/3897873

Nishida, K. (2017). Ambient seismic wave field. *Proceedings of the Japan Academy, Series B, 93*(7), 423-448.

Nishida, K., & Takagi, R. (2016). Teleseismic S wave microseisms. *Science, 353*(6302), 919-921. https://doi.org/10.1126/science.aaf7573

Nolet, G., & Dorman, L. M. (1996). Waveform analysis of Scholte modes in ocean sediment layers. *Geophysical Journal International, 125*(2), 385-396. https://doi.org/10.1111/j.1365-246X.1996.tb00006.x

Poli, P., Campillo, M., & Pedersen, H. (2012). Body-Wave Imaging of Earth's Mantle Discontinuities from Ambient Seismic Noise. *Science, 338*(6110), 1063. https://doi.org/10.1126/science.1228194

Posey, R., Johnson, G. A., & Vohra, S. T. (2000). Strain sensing based on coherent Rayleigh scattering in an optical fibre. *Electronics Letters, 36*(20), 1688-1689. Retrieved from https://doi.org/10.1049/el:20001200

Retailleau, L., & Gualtieri, L. (2021). Multi-phase seismic source imprint of tropical cyclones. *Nature Communications, 12*(1), 2064. https://doi.org/10.1038/s41467-021-22231-y

Scholte, J. G. J. (1958). *Rayleigh Waves in Isotropic and Anisotropic Elastic Media*, Staatsdr.- en Uitgeverijledrijf. https://books.google.com/books?id=ETNHGQAACAAJ

Schweitzer, J., Fyen, J., Mykkeltveit, S., Kværna, T., & Bormann, P. (2002). Seismic arrays. *IASPEI new manual of seismological observatory practice*, 1-51.

Shapiro, N. M., Campillo, M., Stehly, L., & Ritzwoller, M. H. (2005). High-resolution surface-wave tomography from ambient seismic noise. *Science, 307*(5715), 1615-1618. http://doi.org/10.1126/science.1108339

Sladen, A., Rivet, D., Ampuero, J. P., De Barros, L., Hello, Y., Calbris, G., & Lamare, P. (2019). Distributed sensing of earthquakes and ocean-solid Earth interactions on seafloor telecom cables. *Nature Communications, 10*(1), 5777. https://doi.org/10.1038/s41467-019-13793-z

Spica, Z. J., Gaite, B., & Ruiz-Barajas, S. (2020). The Valencia-Islalink Distributed Acoustic Sensing Experiment [Data set]. *PubDAS*. https://doi.org/10.7914/SN/ZH_2020

Spica, Z. J., Nishida, K., Akuhara, T., Pétrélis, F., Shinohara, M., & Yamada, T. (2020). Marine Sediment Characterized by Ocean-Bottom Fiber-Optic Seismology. *Geophysical Research Letters, 47*(16), e2020GL088360. https://doi.org/10.1029/2020GL088360

Tanimoto, T. (2007). Excitation of microseisms. *Geophysical Research Letters*, *34*(5).
Toksöz, M. N., & Lacoss, R. T. (1968). Microseisms: Mode Structure and Sources. *Science*, *159*(3817), 872-873. https://doi.org/10.1126/science.159.3817.872
Tolman, H. L. (2009). User manual and system documentation of WAVEWATCH III TM version 3.14. *J Technical note, MMAB Contribution*, *276*, 220.
Wiechert, E. (1904). Discussion, Verhandlung der zweiten internationalen seismologischen Konferenz. *Beitrage zur Geophysik*, *2*, 41-43.
Williams, E. F., Fernández-Ruiz, M. R., Magalhaes, R., Vanthillo, R., Zhan, Z., González-Herráez, M., & Martins, H. F. (2019). Distributed sensing of microseisms and teleseisms with submarine dark fibers. *Nature Communications*, *10*(1), 5778. https://doi.org/10.1038/s41467-019-13262-7
Xiao, H., Tanimoto, T., & Xue, M. (2021). Study of S-Wave Microseisms Generated by Storms in the Southeast Australia and North Atlantic. *Geophysical Research Letters*, *48*(15), e2021GL093728. https://doi.org/10.1029/2021GL093728
Xiao, H., Xue, M., Yang, T., Liu, C., Hua, Q., Xia, S., et al. (2018). The Characteristics of Microseisms in South China Sea: Results From a Combined Data Set of OBSs, Broadband Land Seismic Stations, and a Global Wave Height Model. *Journal of Geophysical Research: Solid Earth*, *123*(5), 3923-3942. https://doi.org/10.1029/2017JB015291

Gal, M., Reading, A., Ellingsen, S., Koper, K., & Burlacu, R. (2017). Full wavefield decomposition of high- frequency secondary microseisms reveals distinct arrival azimuths for Rayleigh and Love waves. Journal of Geophysical Research: Solid Earth, 122(6), 4660-4675. https://doi.org/10.1002/2017JB014141

Pyle, M. L., Koper, K. D., Euler, G. G., & Burlacu, R. (2015). Location of high-frequency P wave microseismic noise in the Pacific Ocean using multiple small aperture arrays. Geophysical research letters, 42(8), 2700-2708. https://doi.org/10.1002/2015GL063530

Zhang, J., Gerstoft, P., & Shearer, P. M. (2009). High-frequency P-wave seismic noise driven by ocean winds. Geophysical research letters, 36(9). https://doi.org/10.1029/2009GL037761

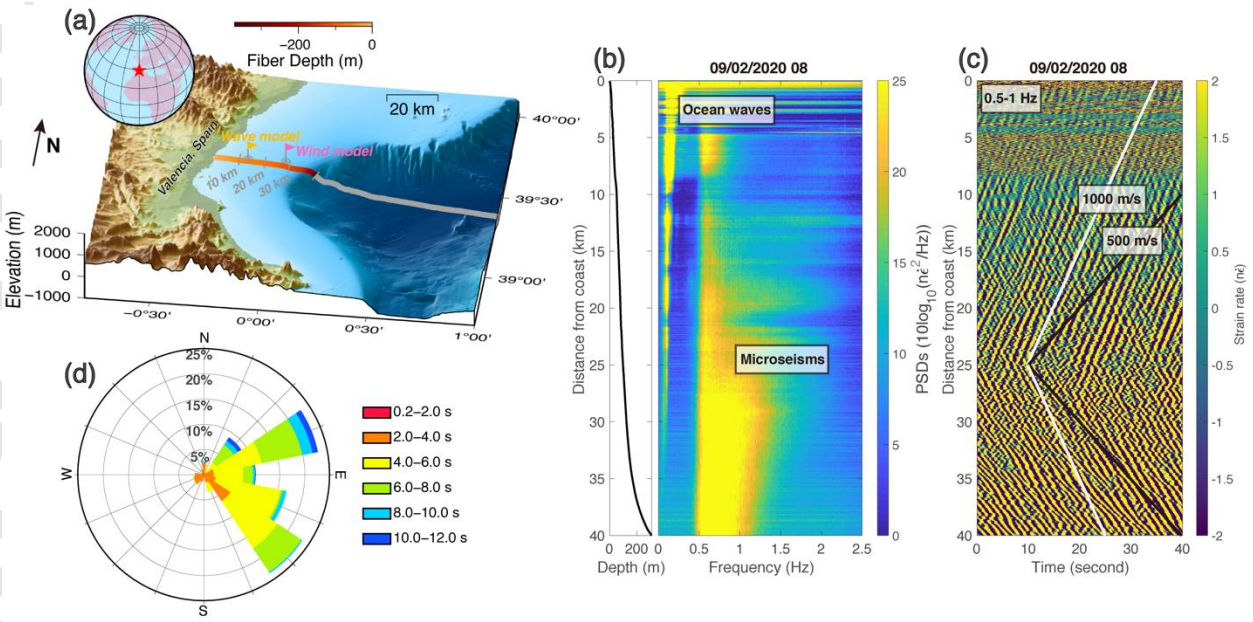


**Figure 1.** DAS, waves, and wind data. (a) The geographic location of the fiber-optic cable in this study. The red line is the portion of the fiber-optic cable we analyzed, and its color represents its depth. The gray line is the portion that was not used. The yellow and pink flags indicate the location of simulated waves and wind, respectively. (b) Power spectral densities of one-hour DAS strain rate data on September 2nd, 2020. (c) Forty seconds of DAS data filtered between 0.5 and 1 Hz along the fiber-optic cable showing HF microseism propagating landward and seaward. (d) Rose of the peak period of ocean waves during September 2020 at the location indicated by the yellow flag in (a). Note that ocean waves propagating in the opposite directions are mainly 2-4 seconds (0.25-0.5 Hz).

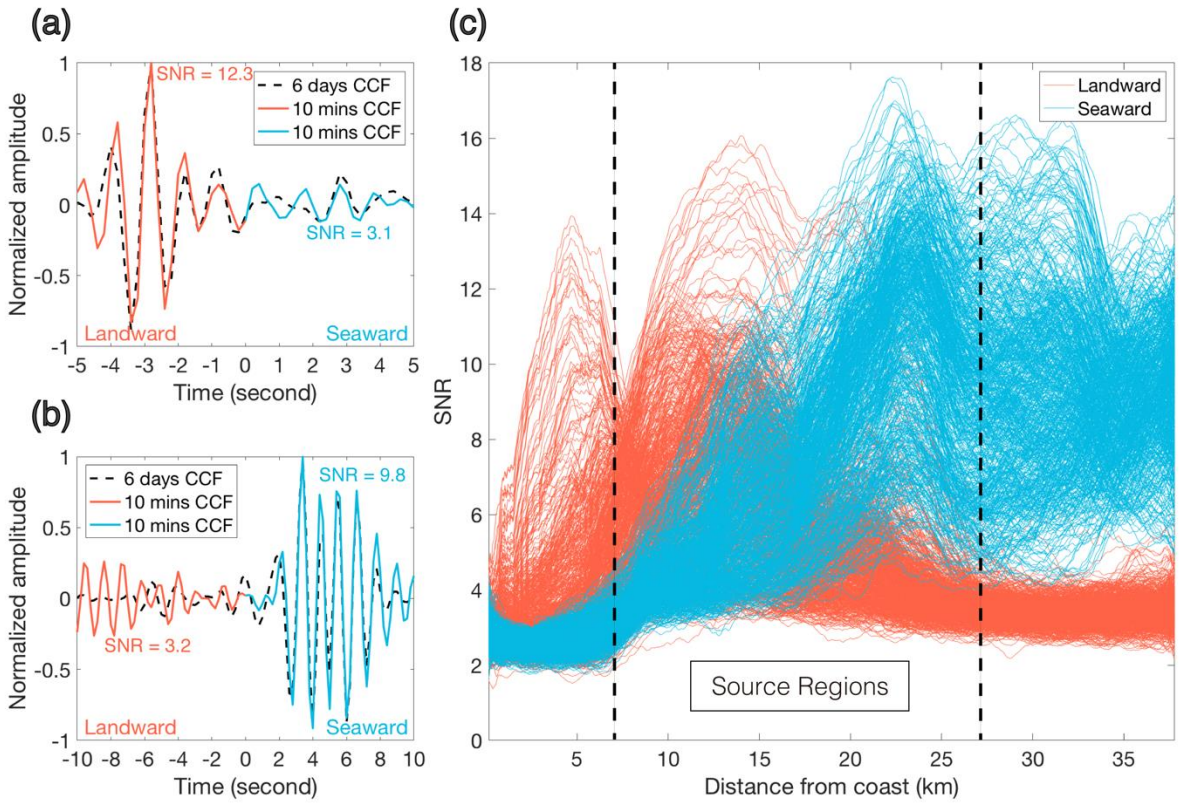


**Figure 2.** Cross-correlation function results. (a) CCF between channels 300-305 (channel 300 is at 5.0 km from the coast) and 390-395 (channel 390 is at 6.5 km from the coast) in the 0.5-1 Hz frequency band. The dashed line shows the 6-day stacked CCF result. The red and blue lines show the 10- minute CCF results. The positive correlation lags (blue line) are the seaward propagation, and the negative lags (red line) are the landward propagation of HF microseism. (b) Same as (a) but for channels 2000-2005 (channel 2000 is at 33.6 km from the coast) and channels 2090-2095 (channel 2090 is at 35.1 km from the coast). (c) SNR of HF microseisms in the frequency band 0.5-1 Hz. Each line represents the SNR variation of the Scholte wave along the fiber, obtained from the 10-minute CCFs. All the results for the 6 days are plotted on this graph. Beyond 27 km from the coast, the seaward propagation dominates, while closer to the coast at 7 km, the landward propagation prevails.

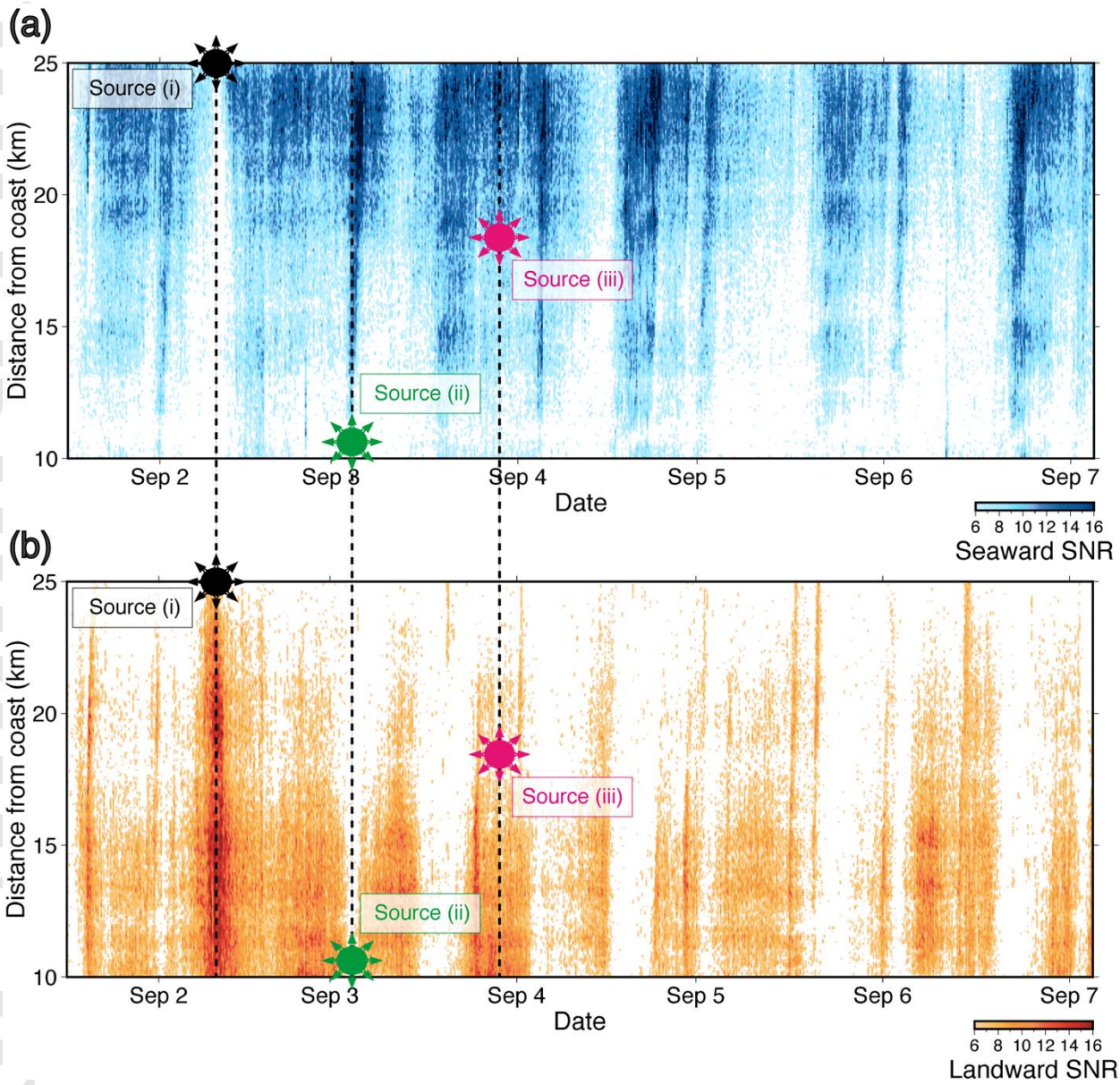


**Figure 3.** Variations in SNR of the HF microseisms. (a) seaward and (b) landward propagations from CCF with SNR higher than 6 and filtered between 0.5 and 1 Hz. The three different colored circles show three representative source locations of the HF microseisms.

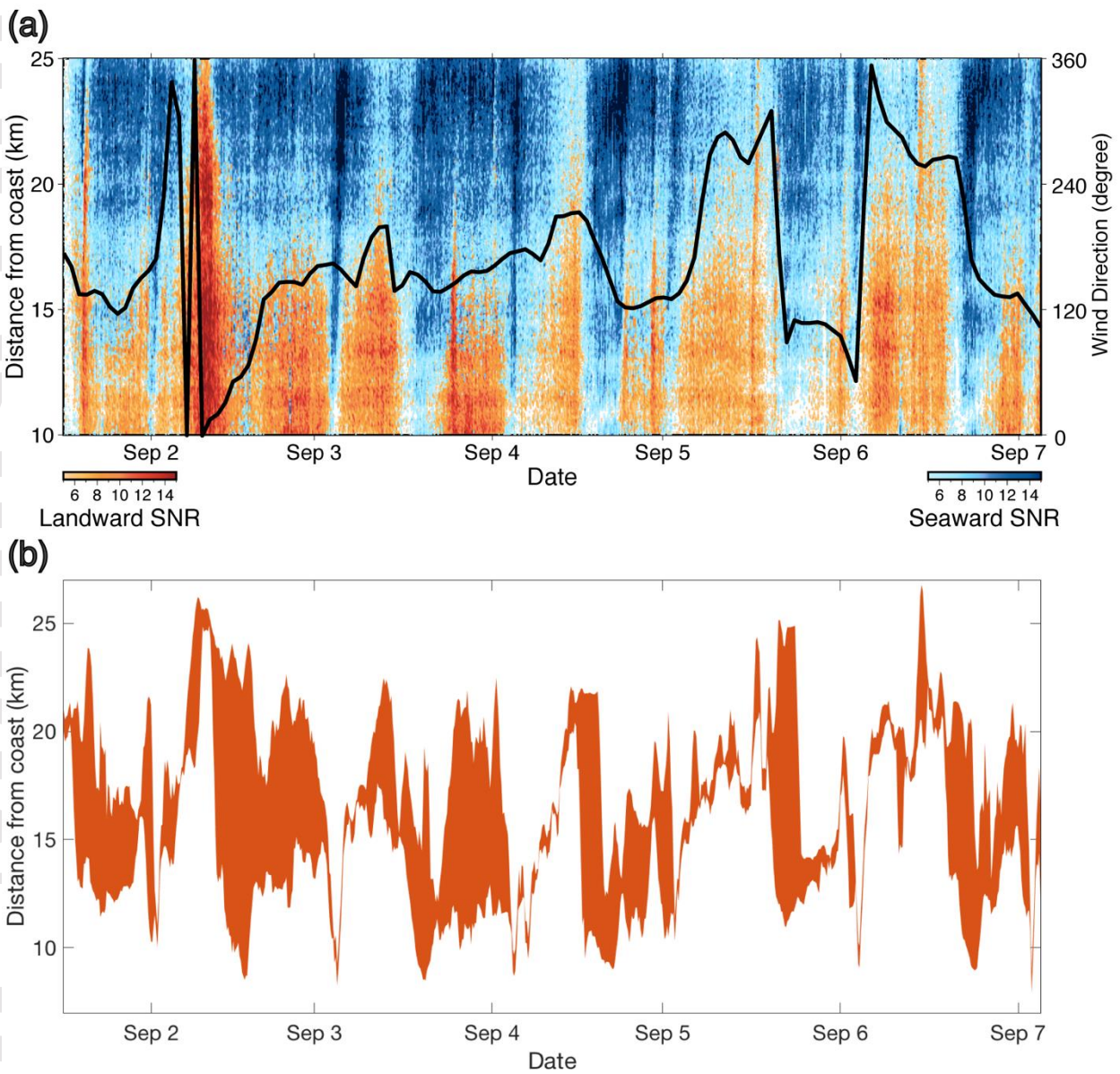


**Figure 4.** HF microseisms source locations. (a) Same data as Figures 3a and 3b but plotted the intersection between the two colors to observe better changes in HF microseism source locations in the frequency band 0.5-1 Hz. The position between the two-color series defines the source locations of HF microseisms. The black line depicts the local wind direction change, measured at the location marked in Figure 1a. The wind direction is from 0° to 360°, where 0° represent absolute north and 180° represent absolute south. (b) The source regions of HF microseisms in the frequency band 0.5-1 Hz. We define the locations of the HF microseism source using a SNR higher than 5 for both seaward and landward propagating Scholte waves.